

Structure-Revealing Low-Light Image Enhancement Via Robust Retinex Model

Mading Li, Jiaying Liu[✉], Senior Member, IEEE, Wenhuan Yang, Xiaoyan Sun, Senior Member, IEEE, and Zongming Guo, Member, IEEE

Abstract—Low-light image enhancement methods based on classic Retinex model attempt to manipulate the estimated illumination and to project it back to the corresponding reflectance. However, the model does not consider the noise, which inevitably exists in images captured in low-light conditions. In this paper, we propose the robust Retinex model, which additionally considers a noise map compared with the conventional Retinex model, to improve the performance of enhancing low-light images accompanied by intensive noise. Based on the robust Retinex model, we present an optimization function that includes novel regularization terms for the illumination and reflectance. Specifically, we use ℓ_1 norm to constrain the piece-wise smoothness of the illumination, adopt a fidelity term for gradients of the reflectance to reveal the structure details in low-light images, and make the first attempt to estimate a noise map out of the robust Retinex model. To effectively solve the optimization problem, we provide an augmented Lagrange multiplier based alternating direction minimization algorithm without logarithmic transformation. Experimental results demonstrate the effectiveness of the proposed method in low-light image enhancement. In addition, the proposed method can be generalized to handle a series of similar problems, such as the image enhancement for underwater or remote sensing and in hazy or dusty conditions.

Index Terms—Low-light image enhancement, Retinex model, structure-revealing, noise suppression.

I. INTRODUCTION

IMAGES captured under low-light conditions suffer from many degradations, such as low visibility, low contrast, and high-level noise. Although these degradations can be somewhat alleviated by professional devices and advanced photographic skills, the inherent cause of the noise is inevitable and cannot be addressed at the hardware level. Without sufficient amount of light, the output of camera sensors is often buried in the intrinsic noise in the system. Longer exposure time can effectively increase the signal-to-noise ratio (SNR)

Manuscript received June 17, 2017; revised November 17, 2017, January 13, 2018, and February 13, 2018; accepted February 14, 2018. Date of publication February 28, 2018; date of current version March 21, 2018. This work was supported in part by the National Natural Science Foundation of China under Contract 61772043 and in part by Microsoft Research Asia under Project ID FY17-RES-THEME-013. The associate editor coordinating the review of this manuscript and approving it for publication was Dr. Alin M. Achim. (*Corresponding author: Jiaying Liu.*)

M. Li, J. Liu, W. Yang, and Z. Guo are with the Institute of Computer Science and Technology, Peking University, Beijing 100871, China (e-mail: martinli0822@pku.edu.cn; lijiaying@pku.edu.cn; yangwenhan@pku.edu.cn; guozongming@pku.edu.cn).

X. Sun is with Internet Media Group, Microsoft Research Asia, Beijing 100080, China (e-mail: xysun@microsoft.com).

Color versions of one or more of the figures in this paper are available online at <http://ieeexplore.ieee.org>.

Digital Object Identifier 10.1109/TIP.2018.2810539

and generate a noise-free image, however it breeds new problems such as motion blur. Thus, low-light image enhancement technique at the software level is highly desired in consumer photography. Moreover, such technique can also benefit many computer vision algorithms (object detection, tracking, etc.) since their performance highly relies on the visibility of the target scene.

However, this is not a trivial task, for that images captured under low-light conditions have rather low SNRs, which means the noises are highly intensive and may dominate over the image signals. Thus, low-light image enhancement algorithms need to tackle not only the low visibility, but also the high-level noises, in addition to low contrast.

An intuitive way to enhance low-light images is to directly amplify the illumination. However, relatively bright areas may be saturated and some details might be lost through the operation. Histogram equalization (HE) based methods [1], [2], which aim to stretch the dynamic range of the observed image, can mitigate the problem to some extent. Nevertheless, their purpose is to enhance the contrast other than adjusting the illumination. Thus, results of these methods may be over- or under-enhanced. Furthermore, HE based methods neglect the intensive noise hidden in low-light images.

Some researchers [3], [4] noticed that the inverted low-light images look like haze images. Dehazing methods are therefore applied and the dehazing result is inverted once more as the enhancement result. A joint-bilateral filter is applied in [4] to suppress the noise after the enhancement. Li *et al.* [3] attempted to further improve the visual quality by segmenting the observed image into superpixels and adaptively denoising different segments via BM3D [5]. Although these methods can generate reasonable results, a convincing physical explanation of their basic model has not been provided. Moreover, the order of enhancing and denoising has always been a problem. Performing enhancement method before denoising may result in noise amplification, which increases the difficulty of denoising. On the other hand, enhancement results may be somewhat blurred after denoising.

In recent years, learning based image enhancement methods have also been studied. Yang *et al.* [6] presented a low light image enhancement method using coupled dictionary learning. Lore *et al.* [7] proposed a Low-Light Net (LLNet) using deep autoencoders to simultaneously (or sequentially) perform contrast enhancement and denoising. In both works, low-light data used for training is synthesized by applying gamma correction on natural image patches since real data paired with low-light and normal illumination is hard to collect. However,

1057-7149 © 2018 IEEE. Personal use is permitted, but republication/redistribution requires IEEE permission.
See http://www.ieee.org/publications_standards/publications/rights/index.html for more information.

such measurement may not fully characterize the formation of natural low-light images, which may lead to unnatural results.

Retinex theory [8] has been studied extensively in the past few decades, which assumes that images can be decomposed into two components, namely reflectance and illumination. Single-scale Retinex [9] and multiscale Retinex [10] are the pioneering studies in this field, which treat the reflectance component as the final output. Wang *et al.* [11] proposed a bright-pass filter to decompose the observed image into reflectance and illumination, and attempted to preserve the naturalness while enhancing the image details. Based on the bright-pass filter proposed in [11], Fu *et al.* [12] fused multiple derivatives of the estimated illumination to combine different merits into a single output. The method proposed in [13] refines the initial illumination map by imposing a structure-aware prior. Nevertheless, due to the lack of constraint on the reflectance, these methods often amplify the latent intensive noise that exists in low-light images.

Although the logarithmic transformation is widely adopted for the ease of modeling by most Retinex based algorithms, a recent work [14] argues that the logarithmic transformation is not appropriate in the regularization terms since pixels with low magnitude dominate over the variation term in the high magnitude areas. Thus, a weighted variational model is proposed in [14] in order to impose better prior representation in the regularization terms. Even though this method shows rather impressive results in the decomposition of reflectance and illumination, the method is not suitable for the enhancement of low-light images as the noise often appears in low magnitude regions.

In this paper, we follow the conventional methods that manipulate the illumination component after the decomposition in order to re-light the input low-light image. In the following sections, we first point out that existing Retinex-based methods using logarithmic transformation are not suitable for handling intensive noise hidden in low-light images. Then, based on the robust Retinex model with an additional noise term, we present the proposed structure-revealing low-light image enhancement method. The method simultaneously estimates a structure-revealed reflectance and a smoothed illumination component (and a noise map if the alternative optimization function is used). The augmented Lagrange multiplier based algorithm is provided to solve the optimization problem. Without sophisticated patch-based techniques such as nonlocal means and dictionary learning, the proposed method presents remarkable results via simply using the refined Retinex model without logarithmic transformation regularized by few common terms. In summary, the contributions of this paper lie in three aspects:

- In this paper, we consider the noise term in the classic Retinex model in order to better formulate images captured under low-light conditions. Based on the model, we make the first attempt to explicitly predict the noise map out of the robust Retinex model, while simultaneously estimate a structure-revealed reflectance map and a piece-wise smoothed illumination map.
- An augmented Lagrange multiplier based alternating direction minimization algorithm without logarithmic

transformation is provided to optimize the objective function.

- The proposed method can also be applied to other practical applications in addition to low-light image enhancement, such as underwater image enhancement, remote sensing image enhancement, image dehazing, and dusty weather image

The rest of this paper is organized as follows. In Sec. II, we briefly review the conventional Retinex model, discuss its drawback for low-light image enhancement, and present the robust Retinex model. Sec. III presents the proposed method based on the robust Retinex model. Experimental results are demonstrated in Sec. IV. Sec. V concludes the paper.

II. BACKGROUND

The classic Retinex model decomposes images into reflectance and illumination:

$$\mathbf{I} = \mathbf{R} \circ \mathbf{L}, \quad (1)$$

where \mathbf{I} is the observed image, \mathbf{R} and \mathbf{L} represent the reflectance and the illumination of the image, respectively. The operator \circ denotes the element-wise multiplication. Most of the existing Retinex-based methods utilize the logarithmic transformation to reduce computational complexity [15].

Image intrinsic decomposition based methods are also able to estimate illumination and reflectance [16]–[20]. However, these methods are mostly based on the assumptions that light sources are distant from the examined scene and the scene does not have multiple dominant illuminating colors, which do not hold in most low-light images (as can be observed in Figs. 9 and 10). Thus, in this paper, we focus on Retinex-based decomposition, and we argue that the classic Retinex model in (1) is not suitable for the low-light image enhancement problem, for that intensive noise inevitably exists in low-light images.

We present the robust Retinex model and point out that the model for the particular task should have a noise term \mathbf{N} as follows:

$$\mathbf{I} = \mathbf{R} \circ \mathbf{L} + \mathbf{N}. \quad (2)$$

This image formulation is similar to that of intrinsic image decomposition, which originally involves three factors including Lambertian shading (\mathbf{L}), reflectance (\mathbf{R}), and specularities (\mathbf{C}). The specular term \mathbf{C} is often used in computer graphics and it accounts for light rays that reflect directly off the surface, which creates visible highlights in the image [16]. For simplicity, many works [16], [21], [22] often neglect the specular component \mathbf{C} . In our work, we still follow this simplification, but a noise term \mathbf{N} is added to the model. Different with the discretely distributed specular term \mathbf{C} , the noise term \mathbf{N} distributes more uniformly in natural images.

Once the noise term is added as in (2), the logarithmic transformation of the classic model becomes questionable. First, since $\log(\mathbf{R}) + \log(\mathbf{L}) \neq \log(\mathbf{R} \circ \mathbf{L} + \mathbf{N})$, the fidelity term in the log-transformed domain $\|(\log(\mathbf{R}) + \log(\mathbf{L})) - \log(\mathbf{I})\|_F^2$ will deviate from the ideal value. Second, the existence of \mathbf{N} may significantly affect the gradient variation in the log-transformed domain. Specifically, taking the reflectance \mathbf{R}

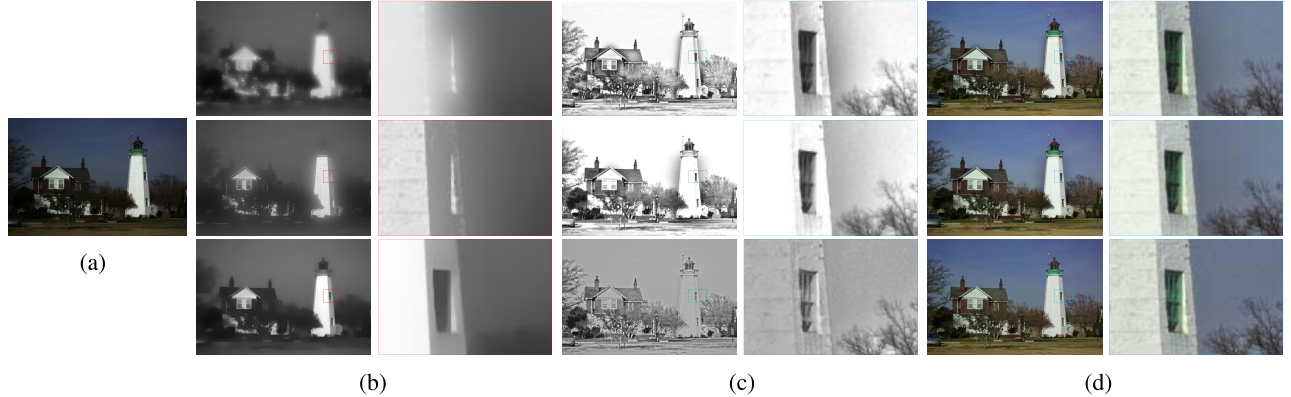


Fig. 1. Comparisons of decomposition results and corresponding enhancement results. From top to bottom: results of SRIE [14], PIE [23], and the proposed method. (a) Input. (b) Illumination. (c) Reflectance. (d) Enhancement.

as an example, its gradient variation in the log-transformed domain $\nabla(\log(\mathbf{R})) = (1/\mathbf{R}) \cdot \nabla\mathbf{R}$ is highly affected by $1/\mathbf{R}$ when \mathbf{R} is very small, which inevitably affects the overall variation term. If \mathbf{R} contains intensive noise, $1/\mathbf{R}$ may become extremely unstable, and the enhancement result may be very noisy, which significantly affects the subjective visual quality. Based on the above analysis, we argue that directly using log-transformed Retinex-model for low-light image enhancement is inappropriate. Thus, in this paper we do not apply logarithmic transformation on Retinex model.

For the particular task of enhancing low-light images, the noise term \mathbf{N} is quite essential. Without it, intensive noise hidden in the observed image \mathbf{I} will eventually be assigned to either \mathbf{L} or \mathbf{R} . As introduced in the previous section, most methods focus on the illumination component \mathbf{L} and regard the reflectance $\mathbf{R} = \mathbf{I}/\mathbf{L}$ as the final output, which inevitably leads to a noisy result. This is the reason why a denoising process is often required after the enhancement [12], [13].

In Retinex based image enhancement methods, some pioneering works have been proposed considering the noise. Elad [24] proposed to constrain the smoothness of both the illumination and the reflectance by two bilateral filters on log-transformed domain. The model handles the proximity of the illumination to the observation and requires the reflectance to be close to the residual image, assuming the noise to be multiplicative. Algorithms proposed in [25] and [26] both consider to directly apply denoising procedures on the estimated reflectance. Li *et al.* [25] employed edge-preserving smoothing [27] while Yu *et al.* [26] used guided filter [28] to suppress the noise in the reflectance map. In this paper, we attempt to enhance the visibility of low-light images and mitigate the effect of noise simultaneously in a joint optimization function, without using logarithmic transformation. The details of our method will be elaborated in the next section.

III. STRUCTURE-REVEALING LOW-LIGHT IMAGE ENHANCEMENT

The proposed structure-revealing low-light image enhancement based on robust Retinex model will be presented in this section. We first give the framework of the proposed method. Then, we introduce two alternative decompositions

to simultaneously estimate the illumination and the reflectance (and the noise) and their solutions are given subsequently.

A. Overview

Following [14] and [23], we perform the proposed method on the V channel in HSV color space. Given the input low-light color image \mathbf{S} , we first convert it into HSV space. Then, the proposed decomposition is applied on the normalized V channel image \mathbf{I} and the illumination component \mathbf{L} and the reflectance component \mathbf{R} can be obtained. After that, in order to light up the dark regions, we adjust the illumination \mathbf{L} and generate an adjusted illumination $\hat{\mathbf{L}}$. The adjusted illumination $\hat{\mathbf{L}}$ is then integrated with the reflectance component \mathbf{R} , producing the enhanced V channel image $\hat{\mathbf{I}}$. Finally, the enhanced HSV image is converted back to RGB color space, and the final enhancement result $\hat{\mathbf{S}}$ is obtained. The details of the proposed structure-revealing low-light image enhancement method will be elaborated in the following subsections.

B. Baseline Decomposition

In this subsection, a new decomposition model that simultaneously estimates the reflectance \mathbf{R} and the illumination \mathbf{L} of the input image \mathbf{I} is formulated as follows:

$$\underset{\mathbf{R}, \mathbf{L}}{\text{argmin}} \|\mathbf{R} \circ \mathbf{L} - \mathbf{I}\|_F^2 + \beta \|\nabla \mathbf{L}\|_1 + \omega \|\nabla \mathbf{R} - \mathbf{G}\|_F^2, \quad (3)$$

where β , and ω are the coefficients that control the importance of different terms. $\|\cdot\|_F$ and $\|\cdot\|_1$ represent the Frobenius norm and ℓ_1 norm, respectively. In addition, ∇ is the first order differential operator, and \mathbf{G} is the adjusted gradient of \mathbf{I} , which will be discussed in Eq. (4). The role of each term in the objective (3) is interpreted below:

- $\|\mathbf{R} \circ \mathbf{L} - \mathbf{I}\|_F^2$ constrains the fidelity between the observed image \mathbf{I} and the recomposed one $\mathbf{R} \circ \mathbf{L}$;
- $\|\nabla \mathbf{L}\|_1$ corresponds to the total variation sparsity and considers the piece-wise smoothness of the illumination map \mathbf{L} ;
- $\|\nabla \mathbf{R} - \mathbf{G}\|_F^2$ minimizes the distance between the gradient of the reflectance \mathbf{R} and \mathbf{G} (an adjusted version of the gradient of the input \mathbf{I}), so that the structural information of the reflectance can be strengthened.

Previous works [14], [23] use an ℓ_2 prior on illumination gradients and an ℓ_1 prior on reflectance gradients. However, we observe that the illumination of most natural low-light images is not uniformly distributed (*i.e.* there exist relatively bright regions), which indicates that using an ℓ_2 norm enforcing a spatially smooth illumination is not appropriate for these images. As can be observed in Fig. 1, previous works generates observable halo artifacts. This is because that ℓ_2 norm generates blurred boundaries around areas where the illumination changes dramatically, which is quite common in low-light images. Even though they use ℓ_1 norm to encourage the piece-wise smoothness of the reflectance, the decomposed reflectance is still affected by the blurred illumination (observed in Fig. 1), as the data fidelity term constrains the product of the illumination and the reflectance to be close to the halo-free input image. Using ℓ_1 prior to constrain illumination gradients as in our work, maintains the overall structure of illumination images and presents better visual quality.

As mentioned in the Sec. I, apart from low visibility and high-level noise, low-light images also suffer from low contrast. Since lower contrast often indicates smaller gradient magnitudes (and vice versa), we attempt to manipulate the gradient magnitudes of the reflectance so that the contrast of the enhancement result can be boosted. To this end, we present the third term $\|\nabla\mathbf{R} - \mathbf{G}\|_F^2$ in our objective function to constrain the fidelity between $\nabla\mathbf{R}$ and a guidance matrix \mathbf{G} . Matrix \mathbf{G} is obtained by amplifying the gradient of the input image with a factor \mathbf{K} . To balance the overall magnitude of \mathbf{G} , the factor \mathbf{K} is designed to adaptively make less (more) adjustment in areas with higher (lower) magnitudes. The formulation of \mathbf{G} is given as follows [29],

$$\mathbf{G} = \mathbf{K} \circ \nabla\mathbf{I}, \quad (4)$$

$$\mathbf{K} = 1 + \lambda e^{-|\nabla\mathbf{I}|/\sigma}. \quad (5)$$

Specifically, $\nabla\mathbf{I}$ is amplified by the factor \mathbf{K} that decreases with the increment of the gradient magnitude. Note that this amplification factor makes less adjustment in areas with higher gradient magnitude, while areas with lower gradient magnitude are strongly enhanced. So that after the amplification, the adjusted gradient \mathbf{G} tends to have similar magnitude. Furthermore, λ controls the degree of the amplification; σ controls the amplification rate of different gradients. In our experiments, parameters λ and σ are all set as 10. For each observed image, matrix \mathbf{G} only needs to be calculated once. Fig. 2(a) and (c) give an example of a pair of enhancement results without and with our contrast constraint term. Fig. 2(b) shows the result obtained by substituting the proposed term $\|\nabla\mathbf{R} - \mathbf{G}\|_F^2$ with $\|\nabla\mathbf{R}\|_F^2$ while keeping the parameters unchanged. It can be observed that structure details in the result with the proposed constraint is clearly revealed.

C. Alternative Decomposition

As stated previously, the existence of noise is inevitable in low-light images. Moreover, the noise observed in natural images is far more complicated than additive white Gaussian noise. Thus, instead of estimating the distribution of the noise,

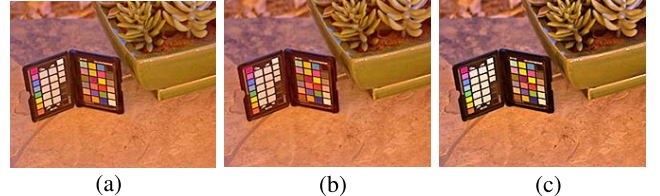


Fig. 2. Comparison of results using different constraint. (a) w/o constraint. (b) $\|\nabla\mathbf{R}\|_F^2$. (c) $\|\nabla\mathbf{R} - \mathbf{G}\|_F^2$.



Fig. 3. Comparisons of results using different models. (a) Input; (b) results generated by the basic model (3); (c) results generated by the alternative model (6); (d) corresponding noise maps (normalized for visualization).

we here attempt to directly estimate a noise map from the input image. In order to explicitly estimate the noise map, we also present the following optimization problem,

$$\begin{aligned} \operatorname{argmin}_{\mathbf{R}, \mathbf{L}, \mathbf{N}} & \|\mathbf{R} \circ \mathbf{L} + \mathbf{N} - \mathbf{I}\|_F^2 + \beta \|\nabla\mathbf{L}\|_1 \\ & + \omega \|\nabla\mathbf{R} - \mathbf{G}\|_F^2 + \delta \|\mathbf{N}\|_F^2, \end{aligned} \quad (6)$$

where \mathbf{N} is the estimated noise map, the term $\|\mathbf{N}\|_F^2$ constrains the overall intensity of the noise. The fidelity term with a noise map is used to guarantee the accuracy of the model, which means that we expect the estimated illumination, reflectance and noise map to accurately reconstruct the input image. As stated in Sec. IV-B.2, the parameters β , ω are significantly smaller than 1 to address the importance of the fidelity term in the optimization.

To avoid amplifying the intensive noise of extremely low-light images, we also modify the formulation of the matrix \mathbf{G} as follows,

$$\mathbf{G} = \mathbf{K} \circ \hat{\nabla}\mathbf{I}, \quad (7)$$

$$\mathbf{K} = 1 + \lambda e^{-|\hat{\nabla}\mathbf{I}|/\sigma}, \quad (8)$$

where

$$\hat{\nabla}\mathbf{I} = \begin{cases} 0, & \text{if } |\nabla\mathbf{I}| < \varepsilon, \\ \nabla\mathbf{I}, & \text{otherwise.} \end{cases} \quad (9)$$

Different with the formulation in Eq. (4), small gradients (*i.e.*, the noise) are suppressed before the amplification.

An example of results generated by different models is shown in Fig. 3. As illustrated, the alternative model (6) efficiently extracts the noise from the input image, and generates result with better visual quality.

D. Solution

Optimization problems (3) and (6) are both non-convex due to $\mathbf{R} \circ \mathbf{L}$. In this paper, we find the alternating direction minimization technique (ADM) efficient solving the problem. Although ADM was first proposed for convex optimizations, there are recent works providing convergence guarantee of ADM for non-convex optimization problems [30], [31]. In practice, we observe that the algorithm converges with reasonable regularization parameters for all the test images (see Sec. IV-D for more details), which also confirms the effectiveness of ADM in our case.

In this subsection, we give the solution of problem (6). The solution of (3) can be obtained similarly.

By substituting $\nabla \mathbf{L}$ in the second term with an auxiliary variable \mathbf{T} , the objective (6) can be rewritten in the following equivalent form:

$$\begin{aligned} \underset{\mathbf{R}, \mathbf{L}, \mathbf{N}, \mathbf{T}}{\operatorname{argmin}} & \| \mathbf{R} \circ \mathbf{L} + \mathbf{N} - \mathbf{I} \|_F^2 + \beta \| \mathbf{T} \|_1 + \delta \| \mathbf{N} \|_F^2 \\ & + \omega \| \nabla \mathbf{R} - \mathbf{G} \|_F^2, \quad \text{s.t.} \quad \mathbf{T} = \nabla \mathbf{L}. \end{aligned} \quad (10)$$

By introducing a Lagrange multiplier \mathbf{Z} to remove the equality constraint, we have the augmented Lagrangian function of (10):

$$\begin{aligned} \mathcal{L}(\mathbf{R}, \mathbf{L}, \mathbf{N}, \mathbf{T}, \mathbf{Z}) = & \| \mathbf{R} \circ \mathbf{L} + \mathbf{N} - \mathbf{I} \|_F^2 + \beta \| \mathbf{T} \|_1 \\ & + \omega \| \nabla \mathbf{R} - \mathbf{G} \|_F^2 + \delta \| \mathbf{N} \|_F^2 \\ & + \Phi(\mathbf{Z}, \nabla \mathbf{L} - \mathbf{T}), \end{aligned} \quad (11)$$

where $\Phi(\mathbf{A}, \mathbf{B}) = \langle \mathbf{A}, \mathbf{B} \rangle + \frac{\mu}{2} \| \mathbf{B} \|_F^2$ and $\langle \cdot, \cdot \rangle$ represents the matrix inner product. μ is a positive scalar. The equivalent objective function can be solved by iteratively updating each variable while regarding other variables that have been estimated in the previous iteration as constants. Here we give the solutions for the k -th iteration of the sub-problems.

• **R sub-problem:** Neglecting the terms unrelated to \mathbf{R} , we have the following optimization problem:

$$\underset{\mathbf{R}}{\operatorname{argmin}} \| \mathbf{L}^{(k)} \circ \mathbf{R} + \mathbf{N}^{(k)} - \mathbf{I} \|_F^2 + \omega \| \nabla \mathbf{R} - \mathbf{G} \|_F^2. \quad (12)$$

We reformulate the first term to make the problem become a classic least squares problem:

$$\underset{\mathbf{R}}{\operatorname{argmin}} \| \tilde{\mathbf{I}}^{(k)} \mathbf{r} + \mathbf{n}^{(k)} - \mathbf{i} \|_F^2 + \omega \| \nabla \mathbf{R} - \mathbf{G} \|_F^2, \quad (13)$$

where \mathbf{I} is the vectorized version of matrix \mathbf{L} and $\tilde{\mathbf{I}}$ represents a diagonal matrix with \mathbf{l} as its entries. The same notation is used with other matrices (\mathbf{r} , \mathbf{i} , \mathbf{n} , \mathbf{t} , \mathbf{g} , and \mathbf{z} correspond to \mathbf{R} , \mathbf{I} , \mathbf{N} , \mathbf{T} , \mathbf{G} , and \mathbf{Z} , respectively). By differentiating (13) with respect to \mathbf{R} and setting the derivative to $\mathbf{0}$, we have the following equation:

$$\begin{aligned} & (\tilde{\mathbf{I}}^{(k)})^T (\tilde{\mathbf{I}}^{(k)} \mathbf{r} + \mathbf{n}^{(k)} - \mathbf{i}) + 2\omega \mathbf{D}^T (\mathbf{D} \mathbf{r} - \mathbf{g}) = \mathbf{0} \\ & \left(f(\tilde{\mathbf{I}}^{(k)}) + \omega f(\mathbf{D}) \right) \mathbf{r} = \tilde{\mathbf{I}}^{(k)} (\mathbf{i} - \mathbf{n}^{(k)}) + \omega \mathbf{D}^T \mathbf{g} \\ & \mathbf{r}^{(k+1)} = \left(f(\tilde{\mathbf{I}}^{(k)}) + \omega f(\mathbf{D}) \right)^{-1} \left(\tilde{\mathbf{I}}^{(k)} (\mathbf{i} - \mathbf{n}^{(k)}) + \omega \mathbf{D}^T \mathbf{g} \right), \end{aligned} \quad (14)$$

where \mathbf{D} is the discrete gradient operator, and $f(\mathbf{x}) = \mathbf{x}^T \mathbf{x}$.

• **L sub-problem:** Collecting the terms related to \mathbf{L} leads to the problem as follows:

$$\underset{\mathbf{L}}{\operatorname{argmin}} \| \mathbf{R}^{(k+1)} \circ \mathbf{L} + \mathbf{N}^{(k)} - \mathbf{I} \|_F^2 + \Phi(\mathbf{Z}^{(k)}, \nabla \mathbf{L} - \mathbf{T}^{(k)}). \quad (15)$$

Similar to the former derivation, we provide the solution of \mathbf{L} as follows:

$$\begin{aligned} \mathbf{l}^{(k+1)} = & \left(2f(\tilde{\mathbf{r}}^{(k+1)}) + \mu f(\mathbf{D}) \right)^{-1} \\ & \times \left(2\tilde{\mathbf{r}}^{(k+1)} (\mathbf{i} - \mathbf{n}^{(k+1)}) + \mu \mathbf{D}^T (\mathbf{t}^{(k)} - \frac{\mathbf{z}^{(k)}}{\mu}) \right). \end{aligned} \quad (16)$$

• **N sub-problem:** Fixing variables other than \mathbf{N} , the problem becomes:

$$\underset{\mathbf{N}}{\operatorname{argmin}} \| \mathbf{R}^{(k+1)} \circ \mathbf{L}^{(k+1)} + \mathbf{N} - \mathbf{I} \|_F^2 + \delta \| \mathbf{N} \|_F^2. \quad (17)$$

The closed form solution for this quadratic problem is given as:

$$\mathbf{N}^{(k+1)} = (\mathbf{I} - \mathbf{R}^{(k+1)} \circ \mathbf{L}^{(k+1)}) / (1 + \delta), \quad (18)$$

where the division is performed element-wise.

• **T sub-problem:** Dropping the terms without \mathbf{T} gives the following problem:

$$\underset{\mathbf{T}}{\operatorname{argmin}} \beta \| \mathbf{T} \|_1 + \Phi(\mathbf{Z}^{(k)}, \nabla \mathbf{L}^{(k+1)} - \mathbf{T}). \quad (19)$$

The solution of (19) can be obtained by performing a shrinkage operation:

$$\mathbf{T}^{(k+1)} = \mathcal{S}_{\frac{\beta}{\mu^{(k)}}} \left(\nabla \mathbf{L}^{(k+1)} + \frac{\mathbf{Z}^{(k)}}{\mu^{(k)}} \right). \quad (20)$$

where $\mathcal{S}_\varepsilon(\mathbf{x}) = \text{sign}(\mathbf{x}) \max(|\mathbf{x}| - \varepsilon, 0)$, in which the calculations are performed element-wise.

• **Updating Z and μ :** The auxiliary matrix \mathbf{Z} and the penalty scalar μ are updated through:

$$\begin{aligned} \mathbf{Z}^{(k+1)} &= \mathbf{Z}^{(k)} + \mu^{(k)} \left(\nabla \mathbf{L}^{(k+1)} - \mathbf{T}^{(k+1)} \right), \\ \mu^{(k+1)} &= \mu^{(k)} \rho, \quad \rho > 1. \end{aligned} \quad (21)$$

The whole iteration is stopped only if the difference between $\mathbf{R}^{(k)}$ and $\mathbf{R}^{(k+1)}$ (or the difference between $\mathbf{L}^{(k)}$ and $\mathbf{L}^{(k+1)}$) is smaller than a threshold, say 10^{-3} in practice, or if the maximal number of iterations is reached.

The entire procedure of the solution to optimization problem (6) is summarized in Algorithm 1, which also includes our initializations of different variables.

E. Illumination Adjustment

After the estimation of the illumination and the reflectance components \mathbf{L} and \mathbf{R} , the final task is to adjust \mathbf{L} to improve the visibility of the input image. In our work, Gamma correction is applied in order to adjust the illumination. The enhanced V channel image $\hat{\mathbf{I}}$ is generated by:

$$\begin{aligned} \hat{\mathbf{I}} &= \mathbf{R} \circ \hat{\mathbf{L}}, \\ \hat{\mathbf{L}} &= \mathbf{L}^{\frac{1}{\gamma}}, \end{aligned} \quad (22)$$

Algorithm 1: The Solution of Problem (10)

Input: The input image \mathbf{I} , the adjusted gradient \mathbf{G} .
Initialization: $\mathbf{L}^{(0)} = \mathbf{I}$, $\mathbf{N}^{(0)} = \mathbf{Z}^{(0)} = \mathbf{T}^{(0)} = \mathbf{0}$, $k = 0$, $\mu^{(0)} = 1$, $\rho = 1.5$.
while not converged **do**
 Update $\mathbf{R}^{(k+1)}$ via Eq. (14);
 Update $\mathbf{L}^{(k+1)}$ via Eq. (16);
 Update $\mathbf{N}^{(k+1)}$ via Eq. (18);
 Update $\mathbf{T}^{(k+1)}$ via Eq. (20);
 Update $\mathbf{Z}^{(k+1)}$ and $\mu^{(k+1)}$ via Eq. (21);
 $k = k + 1$;
end
Output: $\mathbf{R}^{(k)}$, $\mathbf{L}^{(k)}$, $\mathbf{N}^{(k)}$.

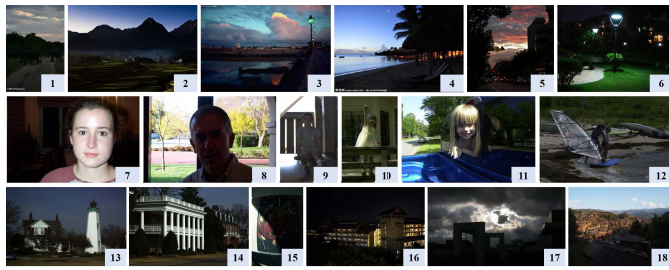


Fig. 4. 18 test images used in our experiments. They are denoted as 1 to 18.

where γ is empirically set as 2.2. Please note that the illumination does not need a normalization before Gamma correction since the input V channel image \mathbf{I} is already normalized to $[0, 1]$. Finally, the enhanced HSV image is transformed to RGB color space, and we have the final enhancement result $\hat{\mathbf{S}}$.

IV. EXPERIMENTAL RESULTS

In this section, we evaluate the performance of the proposed method. First, we present our experiment settings. Then, we evaluate the proposed method by comparing it with state-of-the-art low-light image enhancement methods in both subjective and objective aspects. Noise suppression results are presented afterwards. Then, we conduct an extensive parameter study to evaluate the impact of regularization parameters. Finally, we discuss the computational complexity of our method, and provide experiments on other similar applications.

A. Experiment Settings

To fully evaluate the proposed method, we test our method on images from various scenes. Test images come from the dataset provided by Wang *et al.* [11] and Guo *et al.* [13], frontal face dataset [32], and NASA image dataset [33]. Fig. 4 shows the 18 images tested in our experiments.

All experiments are conducted in MATLAB R2015b on a PC running Windows 10 OS with 64G RAM and 3.5GHz

CPU. In our experiments, if not specifically stated, the parameters β , ω and δ are set as 0.05, 0.01 and 1, respectively. Parameters λ and σ in Eq. (4) are both set to be 10. In most cases, these empirical setting generates decent results.

B. Low-Light Image Enhancement

1) Low-Light Image Enhancement With Less Noise: We compare the proposed method with several state-of-the-art methods, including histogram equalization (HE), naturalness preserved enhancement algorithm (NPE) [11], PIE [23], SRIE [14], and low-light image enhancement via illumination map estimation (LIME) [13]. HE is performed by using the MATLAB built-in function *histeq*. The results of NPE, PIE, SRIE, and LIME are generated by the code downloaded from the authors' websites, with recommended experiment settings.

a) Subjective comparisons: Figs. 5, 6, 7 show several comparisons between enhancement results generated by different methods. Red arrows on these figures indicate noticeable artifacts. HE attempts to stretch the narrowly distributed histograms of low-light images in order to enhance the contrast. However, this method produce noticeable artifacts in flat regions as the continuous values of adjacent pixels are stretched apart. For instance, the sky regions in image #18 (observed in Fig. 5) and image #13 (observed in Fig. 6). Our method, by contrast, can generate artifact-free images with visually pleasing appearance.

As discussed previously, SRIE and PIE generates observable halo artifacts in some regions, such as the halo around the tower in image #13 (observed in Fig. 6). Also, SRIE and PIE cannot sufficiently improve the visibility of the input image, as can be observed in the bottom of image #18 (Fig. 5). In contrast, our method can avoid halo artifacts and produces satisfying results in most cases.

NPE is designed to preserve the naturalness of images, and most of its results have vivid color. But some details in its results are lost, *e.g.* the textures on the lighthouse in image #13 (observed in Fig. 6), the textures on the girl's dress in image #10 (shown in Fig. 7). In fact, among all the compared methods, only the proposed method successfully preserves these textures.

LIME shows impressive performance lighting up dark regions. Nevertheless, this method can easily over-enhance regions with relatively high intensities, such as the dress in image #10 (Fig. 7), textures on the lighthouse in image #13 (Fig. 6). Comparatively, the proposed method produces more natural results, while successfully enhances the visibility of low-light images.

b) Objective quality assessments: Besides subjective visual comparisons, we also apply objective measurements to evaluate the performance of the proposed method objectively. Since assessing the quality of enhanced images is not a trivial task, we adopt three blind quality assessments, *i.e.* no-reference image quality metric for contrast distortion (NIQMC) [34], blind tone-mapped quality index (BTMQI) [35], no-reference free energy based robust metric (NFERM) [36] and a reference based quality assessment,

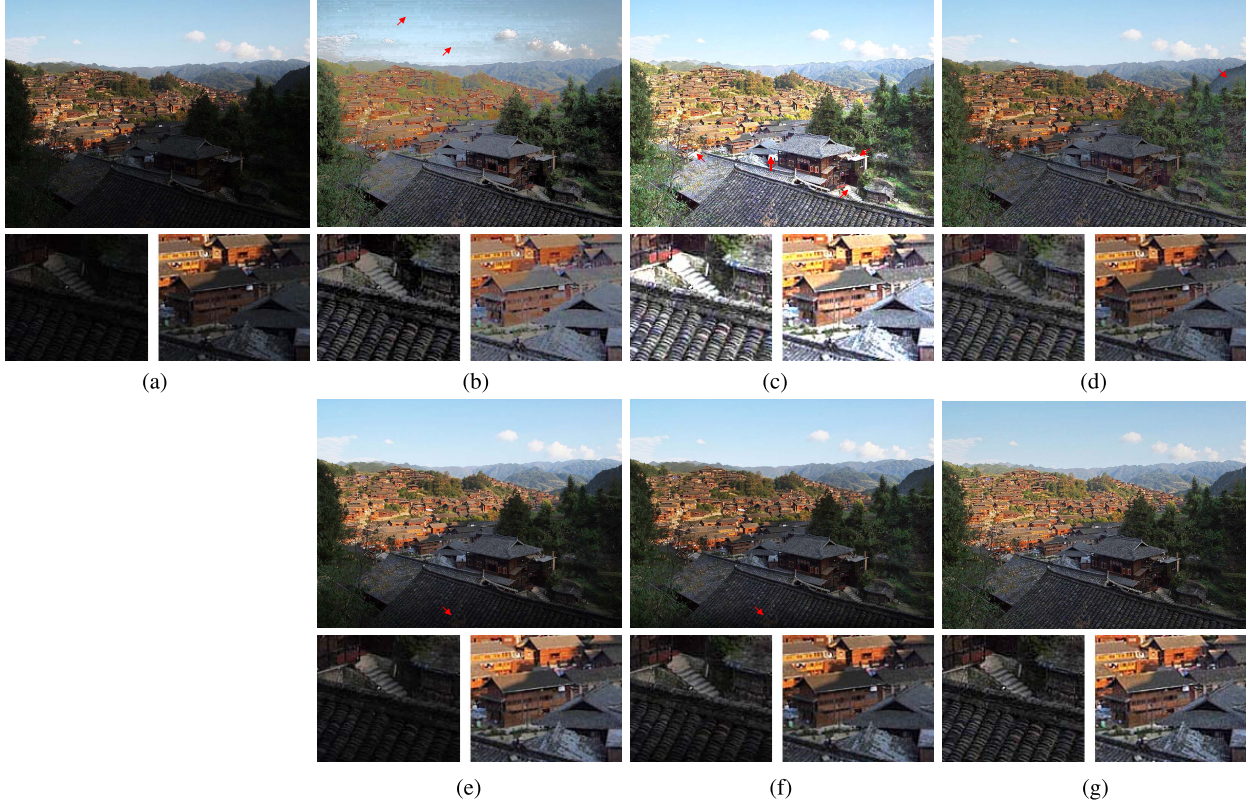


Fig. 5. Comparisons of low-light image enhancement results for test image #18. Red arrows indicate artifacts or degradation. (a) Input. (b) HE. (c) LIME [13]. (d) NPE [11]. (e) PIE [23]. (f) SRIE [14]. (g) Proposed with model (3).

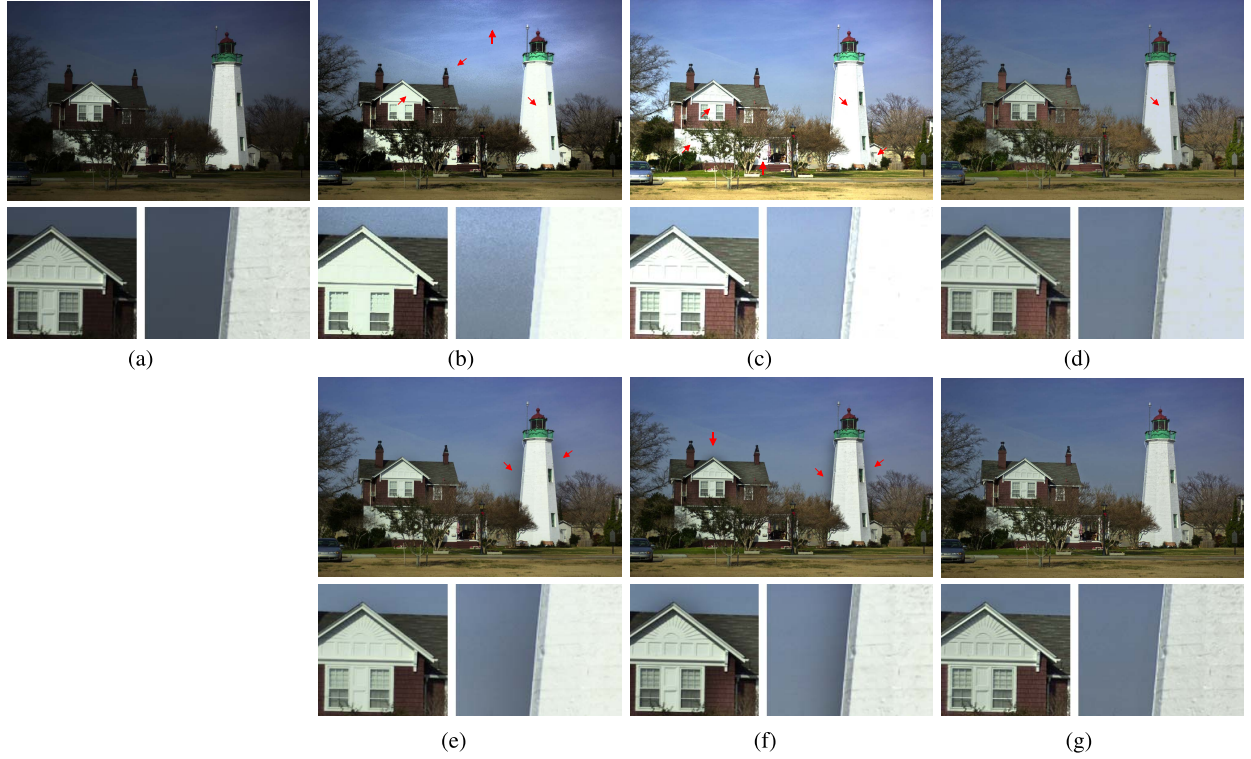


Fig. 6. Comparisons of low-light image enhancement results for test image #13. Red arrows indicate artifacts or degradation. (a) Input. (b) HE. (c) LIME [13]. (d) NPE [11]. (e) PIE [23]. (f) SRIE [14]. (g) Proposed with model (3).

i.e. colorfulness-based patch-based contrast quality index (CPCQI) [37], to evaluate the enhancement results comprehensively. Fig. 8 shows the average NFERM, BTMQI, NIQMC,

and CPCQI results of the input low-light images and the enhancement results generated by aforementioned low-light image enhancement methods.

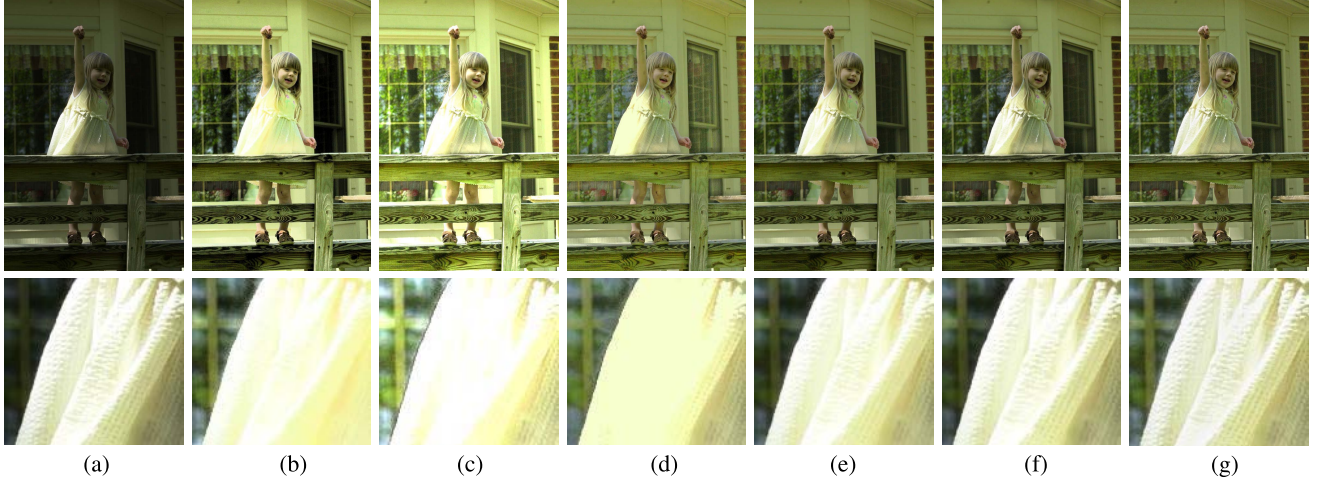


Fig. 7. Comparisons of low-light image enhancement results for test image #10. (a) Input. (b) HE. (c) LIME [13]. (d) NPE [11]. (e) PIE [23]. (f) SRIE [14]. (g) Proposed with model (3).

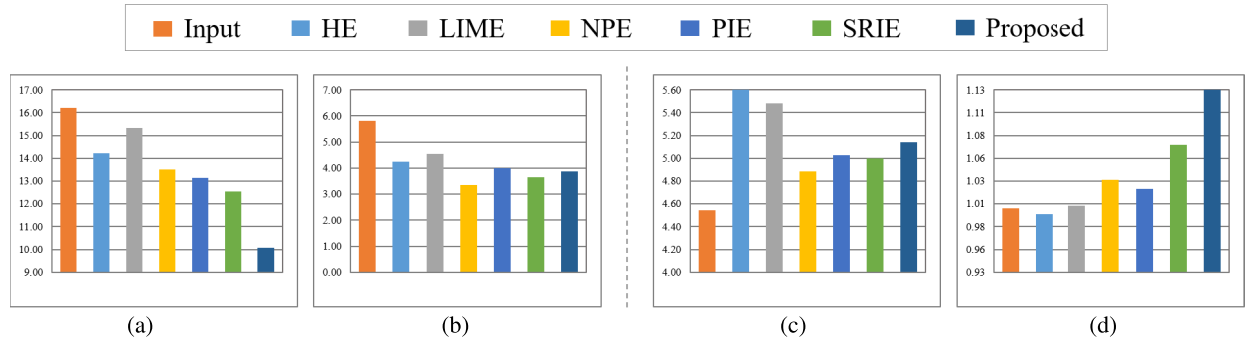


Fig. 8. Average NFERM, BTMQI, NIQMC, and CPCQI results for different methods on all 18 test images with model (3). (a) NFERM. (b) BTMQI. (c) NIQMC. (d) CPCQI.

For NFERM and BTMQI, smaller values represent better image qualities. NFERM extracts features inspired by free energy based brain theory and classical human visual system to measure the distortion of the input image. BTMQI assesses image quality by measuring the average intensity, contrast, and structure information of tone-mapped images. From the figure, we notice that the proposed method achieves the lowest NFERM score, which means that our results are more similar to natural images and have less distortion. The average BTMQI value of the proposed method ranks 3rd among the compared methods. Although NPE and SRIE have lower BTMQI scores, their NFERM values are much larger than that of our method. As can be observed in visual comparisons, some of the results produced by NPE does not look natural, *e.g.* image #18 in Fig. 5 and image #13 in Fig. 6; SRIE cannot fully light up the whole scene (Figs. 5, 9) and generates halo artifacts (Fig. 6).

For CPCQI and NIQMC, larger values indicate better qualities of image contrast. CPCQI evaluates the perceptual distortions between the enhanced image and the input image from three aspects: mean intensity, signal strength and signal structure components. CPCQI value < 1 means that the quality of the enhanced image is degraded rather than enhanced. As can be observed in the figure, the proposed method

achieves the highest CPCQI score, which indicates that our method successfully enhances the overall quality of the image without introducing much artifacts. As for NIQMC, it assesses image quality by measuring local details and global histogram of the given image, and it particularly favors images with higher contrast. It can be observed that HE and LIME have higher NIQMC scores. The reason is that HE and LIME over-enhance the input image. For example, the reflectance on the window in image #10 (shown in Fig. 7), and the lighthouse in image #13 (observed in Fig. 6).

2) Noise Suppression: We evaluate the performance of our low-light image enhancement method under noisy cases using the alternative decomposition described in (6). In this case, noise also exists in other channels apart from the V channel. Thus, the input image is processed in RGB color space and the proposed method is applied in each channel. Parameters β and ω are both set as 0.01 for this task.

Fig. 9 shows some enhancement results of low-light images with intense noise. As can be observed in the figure, the noise hidden in very low-light condition is really intense. Although HE, LIME, and NPE can sufficiently enhance the visibility of low-light images, they also amplify the intensive noise. PIE cannot light up the input images, and its results also contains

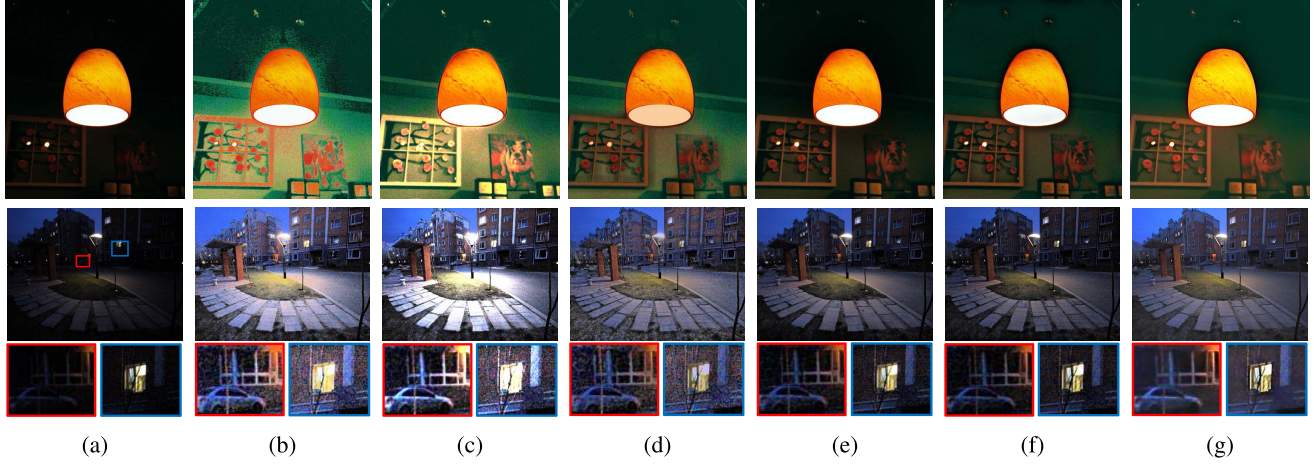


Fig. 9. Comparison of noise suppression. For each case, from left to right, they are the input images, results generated by HE, LIME, NPE, PIE, SRIE, and the proposed method with model (6). (a) Input. (b) HE. (c) LIME [13]. (d) NPE [11]. (e) PIE [23]. (f) SRIE [14]. (g) Proposed.

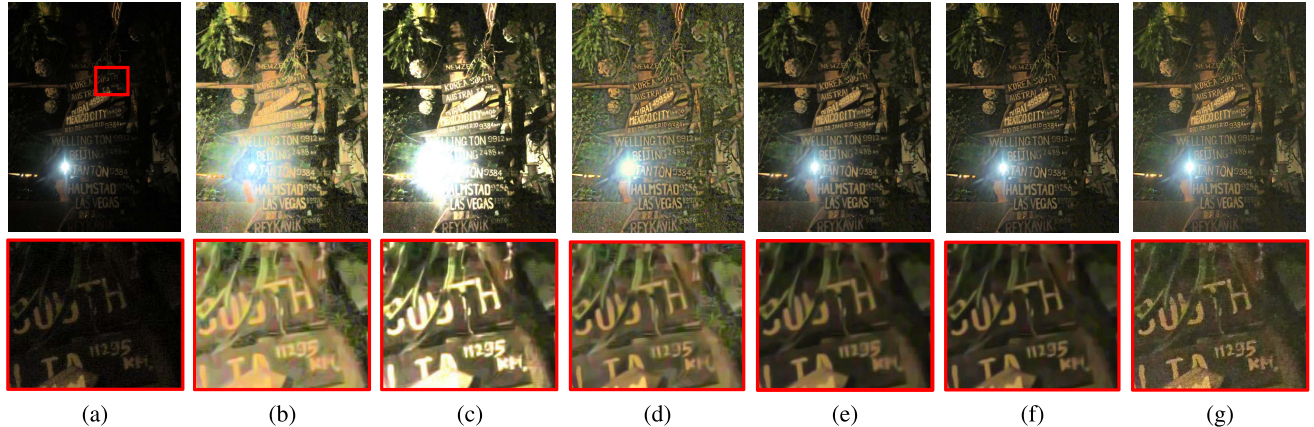


Fig. 10. Comparison of denoising results with the proposed method. (a) is the input image; (b)–(f) are enhancement results of HE, LIME [13], NPE [11], PIE [23], and SRIE [14] with a post-processing performed by BM3D with the denoising parameter $\sigma = 30$; (g) is the result obtained by the proposed method with model (6).

noticeable noise. Our method presents satisfying performance handling low-light images with intensive noise.

We also provide the comparison of the proposed method with the results of other methods post-processed by BM3D [5]. As shown in Fig. 10, the noise amplified by HE and NPE are not properly handled, and many false tiny structures are generated. LIME over-enhanced the input image, especially on regions with higher illumination. Moreover, the denoising process inevitably blurs the whole image. By contrast, our result looks sharper and more natural.

To quantify the effectiveness of our method, we compare with competing method (followed by BM3D) on 200 images from the Berkeley segmentation dataset (BSDS) [38]. We synthesize low-light images by first applying Gamma correction (with $\gamma = 2.2$) on images from BSDS, and then adding Poisson noise and white Gaussian noise to Gamma corrected images. In our work, we use the built-in function of MATLAB *imnoise* to generate Poisson noise. For Gaussian noise, we use $\sigma = 5$ to simulate the noise level in most natural low-light images. Average PSNR and SSIM results of the 200 images by competing methods are listed in Table I, while the best result is highlighted in bold. It can be observed that our

TABLE I
AVERAGE PSNR AND SSIM RESULTS OF DIFFERENT ENHANCEMENT METHODS (FOLLOWED BY BM3D) ON 200 NATURAL COLOR IMAGES FROM BSDS [38]

	HE	LIME	NPE	PIE	SRIE	Proposed
SSIM	0.4277	0.4123	0.4795	0.5076	0.4972	0.5097
PSNR	16.14	15.29	16.72	17.20	16.14	18.53

method achieves the highest PSNR and SSIM values among the competing methods.

3) *Comparison of Different Models:* Generally, our baseline model (3) is more suitable for images without much noise, while the alternative (6) is more effective dealing with low-light images with noise. As can be observed in Fig. 11, compared with the baseline model, the model in (6) effectively remove most of the noise. However, for images with less noise, model (6) may slightly blur some of the tiny details, as shown in the fourth row in Fig. 11 (please observe the details of the roof, the wall and the tree). We also compare results quantitatively using objective criteria NFERM, BTMQI, NIQMC, and CPCQI. For images with less noise

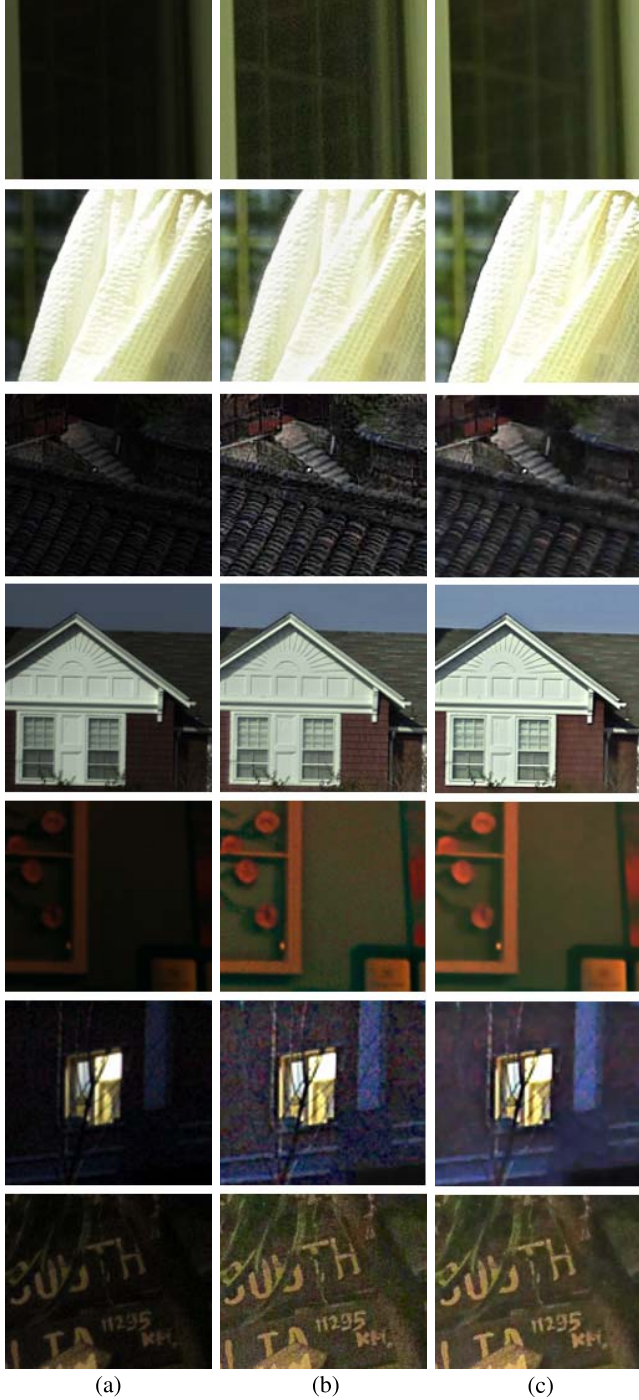


Fig. 11. Comparisons of enhancement result generated by our baseline model (3) and the alternative model (6). (a) Input. (b) Model (3). (c) Model (6).

(18 images shown in Fig. 4), results generated by model (6) obtain averages of 15.60, 3.84, 5.14, and 0.98, which is inferior to that of the baseline model (10.70, 3.87, 5.14, and 1.13). For 200 synthesized noisy images, the average PSNR and SSIM of the baseline model (followed by BM3D) are 18.14 and 0.4632, which is also inferior to that of the model in (6) (18.53 and 0.5097).

To summarize, for images with less noise, our baseline model (3) works fine; for low-light images with noise,

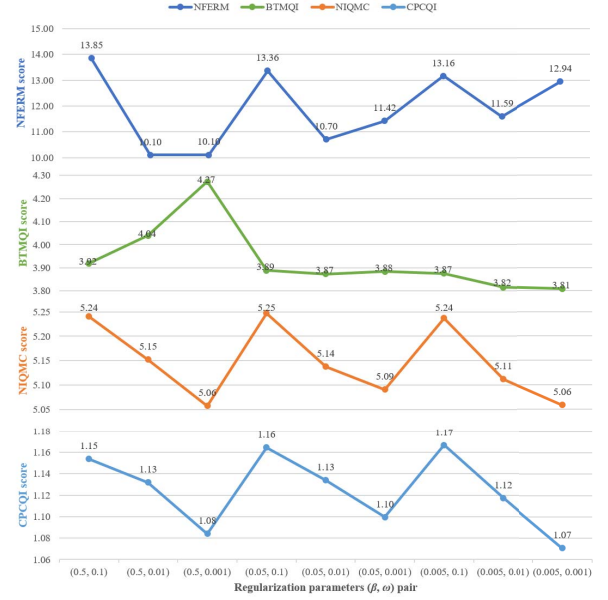


Fig. 12. Average NFERM, BTMQL, NIQMC, and CPCQI results on all 18 test images using the proposed method (the baseline model) with different regularization parameters.

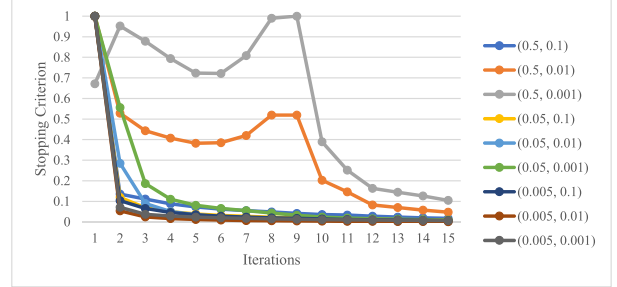


Fig. 13. Convergence speed on image #10 with different regularization parameters using our baseline model.

the model (6) may be a better choice. Combining our models with noise detection/estimation methods and making automatic decisions for which model would be optimal for an input image may be our next research topic.

C. Parameter Study

In this section, we evaluate the effect of regularization parameters. We first evaluate the impact of parameters β and ω in the basic model (3). In Fig. 12, we give objective results obtained with different (β, ω) pairs on all the test images, where β ranges in 0.5, 0.05 and 0.005, and ω is selected from 0.1, 0.01, and 0.001. Please note again that lower NFERM, BTMQL and higher NIQMC, CPCQI values represent better visual quality. As can be observed, results with $(0.5, 0.01)$, $(0.5, 0.001)$, and $(0.05, 0.01)$ have rather low NFERM values. And among them, $(0.05, 0.01)$ has the lowest BTMQL value. From NIQMC and CPCQI values, we can discover a certain pattern with respect to ω .

Fig. 13 plots nine curves, representing different convergence speeds using different (β, ω) pairs on image #10. From the



Fig. 14. Examples of impact of (β, ω) pairs. First row: estimated illumination maps. Second row: estimated reflectance maps. Third row: enhanced images. Default settings are highlighted in bold. The baseline model is used in this case.

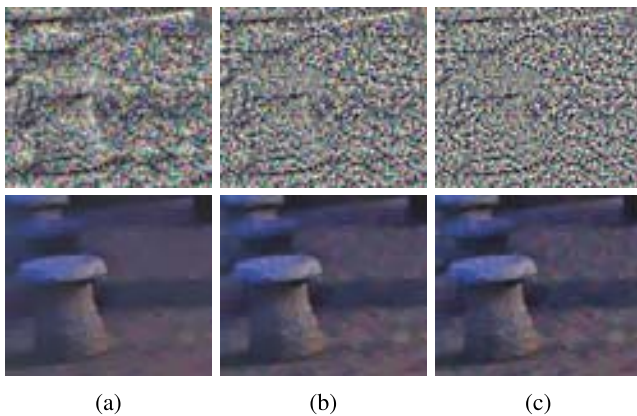


Fig. 15. Examples of parameter impact of δ . First row: estimated noise maps. Second row: enhanced images. Our model (6) is used in this case. (a) $\delta = 0.1$. (b) $\delta = 1$. (c) $\delta = 10$.

curves, we can see that most settings converge within 10 iterations, despite some bumps appeared in $(0.5, 0.01)$ and $(0.5, 0.001)$.

Fig. 14 demonstrate subjective comparisons of the normalized illumination, reflectance, and enhanced results with different (β, ω) pairs on image #10. As can be observed, illumination maps become smoother since the ℓ_1 norm constraint decrease as β increases. The details of estimated reflectance maps are strengthened as ω increases since a larger ω requires the gradient of \mathbf{R} to be more similar to the adjusted gradient \mathbf{G} . In our experiments, we use $(0.05, 0.01)$ as our default setting.

As for the parameter δ in model (6), we vary its value in 0.1, 1, and 10 and demonstrate the results in Fig. 15. From the figure, we can see that a smaller δ over-smooths the result and a larger δ preserves too much noise, which is reasonable since parameter δ constrains the strength of the noise map.

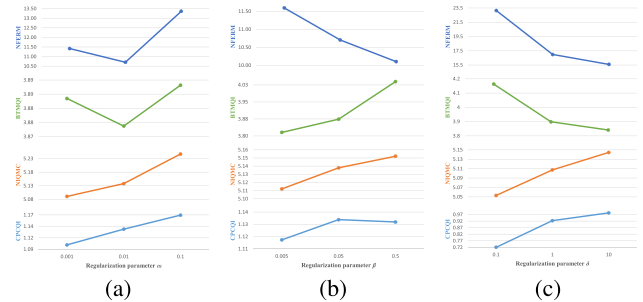


Fig. 16. The effect of different regularization parameters on average NFERM, BTMQI, NIQMC, and CPCQI results using the proposed method for all 18 test images. (a) and (b) are evaluated on the baseline model and (c) on the alternative model. We fix $\beta = 0.05$ in (a), $\omega = 0.01$ in (b), and $\beta = 0.05$, $\omega = 0.01$ in (c).

We further study one parameter each time in Fig. 16. From the figure, we notice several interesting things. First, both NFERM and BTMQI prefer an intermediate ω . Second, NIQMC (who favors higher contrast) always prefers larger parameters. This is consistent with the following observations: a larger β generates a more smooth illumination, which leads to enhancement results with higher contrast (observed in the first and the last column of Fig. 14); a larger ω strengthens the gradients of the enhancement results, which generates results with higher contrast (observed in the third and the fourth column of Fig. 14); compared with a smaller δ that smooths out most of the noise, a larger δ also leads to higher contrast (observed in Fig. 15). Third, in Fig. 16(c), the CPCQI scores are all lower than 1, indicating that the alternative model is not suitable for images with less noise (observed in the fourth row of Fig. 11). Fourth, although all assessment metrics indicate larger δ in Fig. 16(c), we find that a large δ cannot effectively deal with noise (observed in Fig. 15), which is reasonable since δ constrains the intensity of the noise map.

D. Computational Complexity and Convergence Speed

For an image of size 600×400 , HE, LIME, NPE, PIE, SRIE, and the proposed method with the baseline model require about 0.04, 0.41, 10.36, 1.49, 7.64, and 15.67 seconds, respectively. The alternative model in (6) process each channel of input images in RGB color space and takes three times as much as the baseline model. Although the proposed method needs more time, our results are the best in terms of objective and subjective aspects. Also, it should be noticed that since our method is implemented in MATLAB and not well optimized, it could be further accelerated by adopting fast Fourier transformation (FFT) and implementing the code in C/C+++. Fig. 17 plots the convergence curves for all the 18 test images, and gives an intuitive example of the convergence speed of the proposed method. From the curves, we can see that the algorithm converges within 15 iterations for all the 18 test images. In our experiments, we find that setting the maximum number of iterations to be 10 is sufficient to generate satisfying results.

E. Other Applications

It is worth mentioning that, besides low-light image enhancement, the proposed model can also be applied to

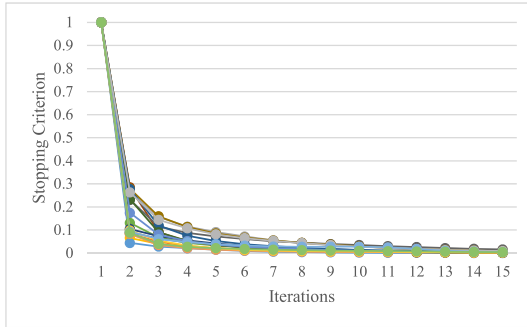


Fig. 17. Convergence curves of the 18 test images with model (3).

a series of degraded images with minor modification. For instance, images captured underwater, haze/fog/smoke images, images taken in dusty weather, remote sensing images can all be enhanced by the proposed method. The formation of haze images is described as follows [39]–[42]:

$$\mathbf{I} = \mathbf{T} \circ \mathbf{J} + \mathbf{A} \circ (1 - \mathbf{T}), \quad (23)$$

where \mathbf{J} is the scene radiance (*i.e.* the desired image with high visibility), \mathbf{A} is the global atmospheric light, and \mathbf{T} is the transmission. In our work, we use the same model for all kinds of degraded images mentioned above. Regarding the inverted illumination component $1 - \mathbf{L}$ obtained by our method as the transmission \mathbf{T} , and with the global atmospheric light \mathbf{A} being set to be a constant 1, the desired image \mathbf{J} can be easily recovered as follows:

$$\mathbf{J} = \frac{\mathbf{I} - \mathbf{L}}{\max(1 - \mathbf{L}, t_0)}. \quad (24)$$

The lower bound t_0 of the transmission is set to be 0.1 as suggested by [42]. In our experiments, to further increase the contrast, \mathbf{J} is multiplied by the reflectance map \mathbf{R} estimated by our method to generate the final result.

Specifically, since images taken in dusty weather and underwater have severe color cast problems, these images are first processed by a simple color correction scheme mentioned in [43] and [44] and then fed to our method. The color corrected image \mathbf{I}_{CR} is calculated by

$$\mathbf{I}_{CR}^c = \frac{\mathbf{I}^c - \mathbf{I}_{\min}^c}{\mathbf{I}_{\max}^c - \mathbf{I}_{\min}^c}, \quad c \in \{R, G, B\} \quad (25)$$

where

$$\begin{aligned} \mathbf{I}_{\max}^c &= \text{mean}(\mathbf{I}^c) + \text{var}(\mathbf{I}^c), \\ \mathbf{I}_{\min}^c &= \text{mean}(\mathbf{I}^c) - \text{var}(\mathbf{I}^c). \end{aligned} \quad (26)$$

$\text{mean}(\mathbf{I}^c)$ is the mean value of \mathbf{I}^c , and $\text{var}(\mathbf{I}^c)$ denotes the variance of \mathbf{I}^c . Figs. 18, 19, and 20 give several enhancement results.

Fig. 18 presents several examples of underwater image enhancement. Test images and the source code of [43] come from the author's website. The specialized underwater image enhancement method [43] utilizes Retinex model to decompose the input image. The decomposed reflectance is enhanced by CLAHE and the illumination is enhanced by histogram specification. The final result is obtained by combining

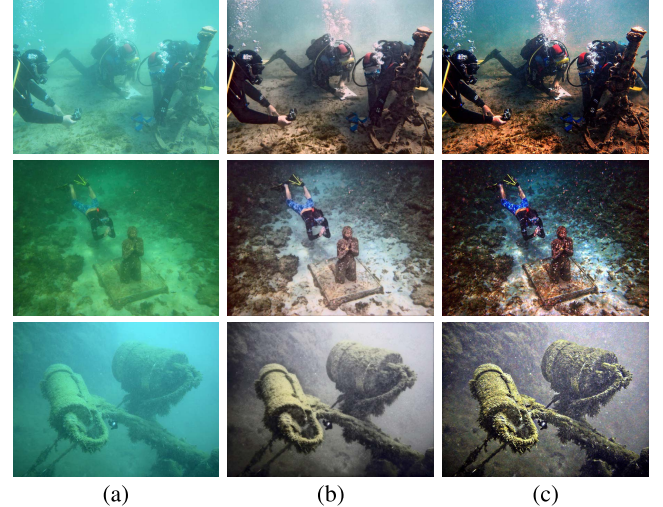


Fig. 18. Comparison of enhancement results of underwater images. From left to right: observed images, results by a specialized method [43] and the proposed method with model (6). (a) Input. (b) Results by [43]. (c) Proposed.

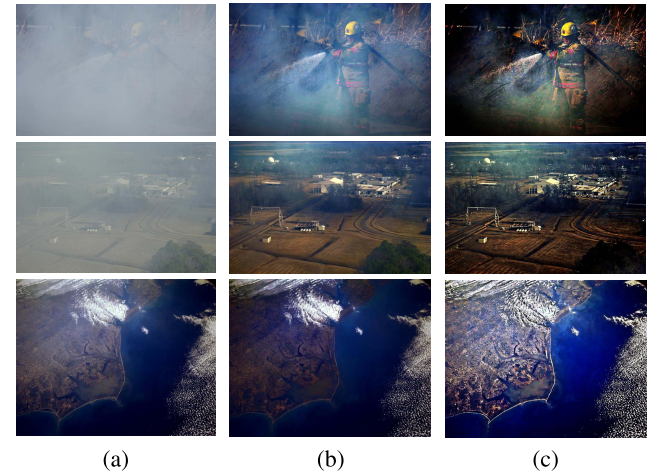


Fig. 19. Comparison of enhancement results of two hazy images taken through thick smoke and a very typical image taken from Earth orbit with low contrast and dark areas. From left to right: observed images, results by the classic dehazing method [42] and the proposed method with model (6). (a) Input. (b) Results by [42]. (c) Proposed.

the two enhanced components by pixel-wise multiplication. As illustrated, compared to the specialized method, our method presents visually appealing results with higher contrast.

Fig. 19 shows some smoke removal/dehazing results. Test images come from the NASA image dataset [33]. Our method is compared with the classic dehazing method [42]. He *et al.* [42] noticed that a major difference between haze-free outdoor images and haze images is that, the minimum intensities on each channel of a haze image tend to have higher value than haze-free images. Thus, they proposed the dark channel prior and used the prior to estimate the transmission map. From the figure, we can see that the method proposed in [42] fails to look through the thick smoke in the first test image, while our method successfully removes most of the smoke. The proposed method also produces higher contrast.

Enhancement results of images taken in dusty weather are illustrated in Fig. 20. Test images and the source code of [44]

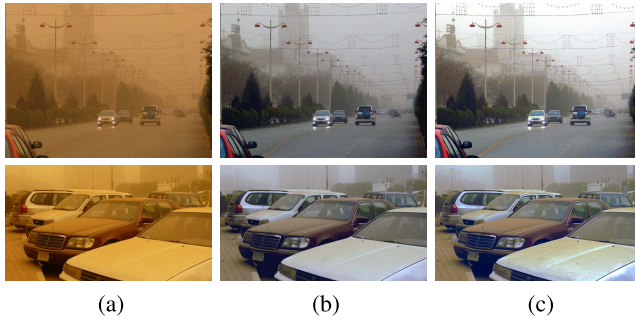


Fig. 20. Comparison of enhancement results of images taken in dusty weather. From left to right: observed images, results by a specialized method [44] and the proposed method with model (6). (a) Input. (b) Results by [44]. (c) Proposed.

are downloaded from the author's website. The specialized method takes different derivatives (generated by Gamma correction with different γ) of the original image as input. Three weight maps (sharpness, chromatic, and prominence maps) calculated from each derivative are summed and normalized to obtain the final weight map, which is then used to fuse the corresponding derivative to obtain the final result. As shown in the figure, results by [44] still look like images with haze, while our method produces images with better visibility.

V. CONCLUSION

Low-light enhancement methods using the classic Retinex model often fail to deal with the noise, which inevitably exists in such condition. In this paper, we present the robust Retinex model by adding a noise term to handle low-light image enhancement in the case of intensive noise. Moreover, we impose novel regularization terms in our optimization problem for both illumination and reflectance to jointly estimate a piece-wise smoothed illumination and a structure-revealed reflectance. An ADM-based algorithm is provided to solve the optimization problem. In addition to low-light image enhancement, our method is also suitable for other similar tasks, such as image enhancement for underwater or remote sensing, and in hazy or dusty conditions. Future works include accelerating our method and generalizing it to video enhancement. Automatically deciding which model would be optimal for an input image is also an appealing topic.

REFERENCES

- [1] S. M. Pizer, R. E. Johnston, J. P. Ericksen, B. C. Yankaskas, and K. E. Muller, "Contrast-limited adaptive histogram equalization: Speed and effectiveness," in *Proc. 1st Conf. Vis. Biomed. Comput.*, May 1990, pp. 337–345.
- [2] M. Abdullah-Al-Wadud, M. H. Kabir, M. A. A. Dewan, and O. Chae, "A dynamic histogram equalization for image contrast enhancement," *IEEE Trans. Consum. Electron.*, vol. 53, no. 2, pp. 593–600, May 2007.
- [3] L. Li, R. Wang, W. Wang, and W. Gao, "A low-light image enhancement method for both denoising and contrast enlarging," in *Proc. IEEE Int. Conf. Image Process.*, Sep. 2015, pp. 3730–3734.
- [4] X. Zhang, P. Shen, L. Luo, L. Zhang, and J. Song, "Enhancement and noise reduction of very low light level images," in *Proc. 21st Int. Conf. Pattern Recognit. (ICPR)*, Nov. 2012, pp. 2034–2037.
- [5] K. Dabov, A. Foi, V. Katkovnik, and K. Egiazarian, "Image denoising by sparse 3-D transform-domain collaborative filtering," *IEEE Trans. Image Process.*, vol. 16, no. 8, pp. 2080–2095, Aug. 2007.
- [6] J. Yang, X. Jiang, C. Pan, and C.-L. Liu, "Enhancement of low light level images with coupled dictionary learning," in *Proc. IEEE 23rd Int. Conf. Pattern Recognit.*, Dec. 2016, pp. 751–756.
- [7] K. G. Lore, A. Akintayo, and S. Sarkar, "LLNet: A deep autoencoder approach to natural low-light image enhancement," *Pattern Recognit.*, vol. 61, pp. 650–662, Jan. 2017.
- [8] E. H. Land, "The retinex theory of color vision," *Sci. Amer.*, vol. 237, no. 6, pp. 108–129, 1977.
- [9] D. J. Jobson, Z.-U. Rahman, and G. A. Woodell, "Properties and performance of a center/surround retinex," *IEEE Trans. Image Process.*, vol. 6, no. 3, pp. 451–462, Mar. 1997.
- [10] D. J. Jobson, Z.-U. Rahman, and G. A. Woodell, "A multiscale retinex for bridging the gap between color images and the human observation of scenes," *IEEE Trans. Image Process.*, vol. 6, no. 7, pp. 965–976, Jul. 1997.
- [11] S. Wang, J. Zheng, H.-M. Hu, and B. Li, "Naturalness preserved enhancement algorithm for non-uniform illumination images," *IEEE Trans. Image Process.*, vol. 22, no. 9, pp. 3538–3548, Sep. 2013.
- [12] X. Fu, D. Zeng, Y. Huang, Y. Liao, X. Ding, and J. Paisley, "A fusion-based enhancing method for weakly illuminated images," *Signal Process.*, vol. 129, pp. 82–96, Dec. 2016.
- [13] X. Guo, Y. Li, and H. Ling, "LIME: Low-light image enhancement via illumination map estimation," *IEEE Trans. Image Process.*, vol. 26, no. 2, pp. 982–993, Feb. 2017.
- [14] X. Fu, D. Zeng, Y. Huang, X.-P. Zhang, and X. Ding, "A weighted variational model for simultaneous reflectance and illumination estimation," in *Proc. IEEE Conf. Comput. Vis. Pattern Recognit.*, Jun. 2016, pp. 2782–2790.
- [15] E. Provenzi, L. De Carli, A. Rizzi, and D. Marini, "Mathematical definition and analysis of the retinex algorithm," *J. Opt. Soc. Amer. A, Opt. Image Sci.*, vol. 22, no. 12, pp. 2613–2621, 2005.
- [16] R. Grossé, M. K. Johnson, E. H. Adelson, and W. T. Freeman, "Ground truth dataset and baseline evaluations for intrinsic image algorithms," in *Proc. IEEE Int. Conf. Comput. Vis.*, Sep/Oct. 2009, pp. 2335–2342.
- [17] Q. Chen and V. Koltun, "A simple model for intrinsic image decomposition with depth cues," in *Proc. IEEE Int. Conf. Comput. Vis.*, Dec. 2013, pp. 241–248.
- [18] P.-Y. Laffont, A. Bousseau, and G. Drettakis, "Rich intrinsic image decomposition of outdoor scenes from multiple views," *IEEE Trans. Vis. Comput. Graph.*, vol. 19, no. 2, pp. 210–224, Feb. 2013.
- [19] S. Bell, K. Bala, and N. Snavely, "Intrinsic images in the wild," *ACM Trans. Graph.*, vol. 33, no. 4, p. 159, 2014.
- [20] A. Meka, M. Zollhöfer, C. Richardt, and C. Theobalt, "Live intrinsic video," *ACM Trans. Graph.*, vol. 35, no. 4, p. 109, 2016.
- [21] J. T. Barron and J. Malik, "Color constancy, intrinsic images, and shape estimation," in *Proc. 12th Eur. Conf. Comput. Vis.*, 2012, pp. 57–70.
- [22] Y. Li and M. S. Brown, "Single image layer separation using relative smoothness," in *Proc. IEEE Conf. Comput. Vis. Pattern Recognit.*, Jun. 2014, pp. 2752–2759.
- [23] X. Fu, Y. Liao, D. Zeng, Y. Huang, X. Zhang, and X. Ding, "A probabilistic method for image enhancement with simultaneous illumination and reflectance estimation," *IEEE Trans. Image Process.*, vol. 24, no. 12, pp. 4965–4977, Dec. 2015.
- [24] M. Elad, "Retinex by two bilateral filters," in *Proc. 5th Int. Conf. Scale Space PDE Methods Comput. Vis.*, 2005, pp. 217–229.
- [25] W.-J. Li, B. Gu, J.-T. Huang, and M.-H. Wang, "Novel retinex algorithm by interpolation and adaptive noise suppression," *J. Central South Univ.*, vol. 19, no. 9, pp. 2541–2547, 2012.
- [26] X. Yu, X. Luo, G. Lyu, and S. Luo, "A novel retinex based enhancement algorithm considering noise," in *Proc. 16th Int. Conf. Comput. Inf. Sci. (ICIS)*, May 2017, pp. 649–654.
- [27] Z. Farbman, D. Lischinski, and R. Szeliski, "Edge-preserving decompositions for multi-scale tone and detail manipulation," *Trans. Graph.*, vol. 27, no. 3, p. 67, Aug. 2008.
- [28] K. He, J. Sun, and X. Tang, "Guided image filtering," *IEEE Trans. Pattern Anal. Mach. Intell.*, vol. 35, no. 6, pp. 1397–1409, Jun. 2013.
- [29] W. Chao and Y. Zhong-Fu, "Variational enhancement for infrared images," *J. Infr. Millim. Waves*, vol. 25, no. 4, pp. 306–310, 2006.
- [30] Y. Wang, W. Yin, and J. Zeng, "Global convergence of ADMM in nonconvex nonsmooth optimization," Dept. Comput. Appl. Math., Univ. California, Los Angeles, CA, USA, Tech. Rep. 62, 2015, vol. 15.
- [31] Y. Xu, W. Yin, Z. Wen, and Y. Zhang, "An alternating direction algorithm for matrix completion with nonnegative factors," *Frontiers Math. China*, vol. 7, no. 2, pp. 365–384, 2012.
- [32] *Image Datasets of the Computational Vision Group at CALTECH*. [Online]. Available: <http://www.vision.caltech.edu/archive.html>

- [33] NASA. (2001). *Retinex Image Processing*. [Online]. Available: <https://dragon.larc.nasa.gov/retinex/pao/news>
- [34] K. Gu, W. Lin, G. Zhai, X. Yang, W. Zhang, and C. W. Chen, "No-reference quality metric of contrast-distorted images based on information maximization," *IEEE Trans. Cybern.*, vol. 47, no. 12, pp. 4559–4565, Dec. 2017.
- [35] K. Gu *et al.*, "Blind quality assessment of tone-mapped images via analysis of information, naturalness, and structure," *IEEE Trans. Multimedia*, vol. 18, no. 3, pp. 432–443, Mar. 2016.
- [36] K. Gu, G. Zhai, X. Yang, and W. Zhang, "Using free energy principle for blind image quality assessment," *IEEE Trans. Multimedia*, vol. 17, no. 1, pp. 50–63, Jan. 2015.
- [37] K. Gu, D. Tao, J.-F. Qiao, and W. Lin, "Learning a no-reference quality assessment model of enhanced images with big data," *IEEE Trans. Neural Netw. Learn. Syst.*, to be published. [Online]. Available: <http://ieeexplore.ieee.org/document/7872424/>
- [38] D. Martin, C. Fowlkes, D. Tal, and J. Malik, "A database of human segmented natural images and its application to evaluating segmentation algorithms and measuring ecological statistics," in *Proc. 8th IEEE Int. Conf. Comput. Vis. (ICCV)*, vol. 2, Jul. 2001, pp. 416–423.
- [39] L. Kratz and K. Nishino, "Factorizing scene albedo and depth from a single foggy image," in *Proc. IEEE 12th Int. Conf. Comput. Vis.*, Sep./Oct. 2009, pp. 1701–1708.
- [40] G. Meng, Y. Wang, J. Duan, S. Xiang, and C. Pan, "Efficient image dehazing with boundary constraint and contextual regularization," in *Proc. IEEE Int. Conf. Comput. Vis.*, Dec. 2013, pp. 617–624.
- [41] J.-P. Tarel and N. Hautiere, "Fast visibility restoration from a single color or gray level image," in *Proc. IEEE 12th Int. Conf. Comput. Vis. (ICCV)*, Sep. 2009, pp. 2201–2208.
- [42] K. He, J. Sun, and X. Tang, "Single image haze removal using dark channel prior," in *Proc. IEEE Int. Conf. Comput. Vis. Pattern Recognit.*, Miami, FL, USA, Jun. 2009, pp. 1956–1963.
- [43] X. Fu, P. Zhuang, Y. Huang, Y. Liao, X.-P. Zhang, and X. Ding, "A retinex-based enhancing approach for single underwater image," in *Proc. IEEE Int. Conf. Image Process.*, Oct. 2014, pp. 4572–4576.
- [44] X. Fu, Y. Huang, D. Zeng, X.-P. Zhang, and X. Ding, "A fusion-based enhancing approach for single sandstorm image," in *Proc. IEEE Int. Workshop Multimedia Signal Process.*, Sep. 2014, pp. 1–5.



Mading Li received the B.S. degree in computer science from Peking University in 2013, where he is currently pursuing the Ph.D. degree with the Institute of Computer Science and Technology, being advised by Z. Guo and J. Liu. He was a Visiting Scholar with McMaster University in 2016. His current research interests include image and video processing, image interpolation, image restoration, and low-light image enhancement.



Jiaying Liu (S'08–M'10–SM'17) received the B.E. degree in computer science from Northwestern Polytechnic University, Xian, China, in 2005, and the Ph.D. degree (Hons.) in computer science from Peking University, Beijing, China, in 2010.

She is currently an Associate Professor with the Institute of Computer Science and Technology, Peking University. She has authored over 100 technical articles in refereed journals and proceedings and holds 24 granted patents. Her current research interests include image/video processing, compression, and computer vision.

Dr. Liu was a Visiting Scholar with the University of Southern California, Los Angeles, CA, USA, from 2007 to 2008. In 2015, she was a Visiting Researcher with Microsoft Research Asia, supported by Star Track for Young Faculties. She served as a TC Member in the IEEE CAS MSA and APSIPA IVM and a APSIPA Distinguished Lecturer from 2016 to 2017. She is a Senior Member of CCF.



Wenhan Yang received the B.S. degree in computer science from Peking University, Beijing, China, in 2012, where he is currently pursuing the Ph.D. degree with the Institute of Computer Science and Technology. He was a Visiting Scholar with the National University of Singapore from 2015 to 2016. His current research interests include image processing, sparse representation, image restoration, and deep-learning-based image processing.



Xiaoyan Sun is currently a Lead Researcher with Microsoft Research Asia. She is currently focusing on video analysis, image restoration, and image/video coding. She has authored or co-authored over 100 papers in journals and conferences, holds ten proposals to standards with one accepted, and holds over ten granted U.S. patents. Her current research interests include computer vision, image/video processing, and machine learning. She is a TC Member of the IEEE Multimedia Systems and Applications. She received the Best Paper Award from the IEEE TRANSACTIONS ON CIRCUITS AND SYSTEMS FOR VIDEO TECHNOLOGY in 2009 and the Best Student Paper Award from VCIP in 2016. She is an AE of the *Signal Processing: Image Communication Journal* and an AE of the *IEEE JOURNAL ON EMERGING AND SELECTED TOPICS IN CIRCUITS AND SYSTEMS*. She also served as the session chair, the area chair, and the TC co-chair for several international conferences.

She received the B.S., M.S., and Ph.D. degrees in computer science from the Harbin Institute of Technology, Harbin, China, in 1997, 1999, and 2003, respectively. She was an Intern with Microsoft Research Asia from 2000 to 2003, and joined Microsoft Research Asia in 2003. She is currently an Adjunct Professor (a Ph.D. Supervisor) with the University of Science and Technology of China.



Zongming Guo (M'09) received the B.S. degree in mathematics and the M.S. and Ph.D. degrees in computer science from Peking University, Beijing, China, in 1987, 1990, and 1994, respectively.

He is currently a Professor with the Institute of Computer Science and Technology, Peking University. His current research interests include video coding, processing, and communication.

Dr. Guo is an Executive Member of the China Society of Motion Picture and Television Engineers. He was a recipient of the First Prize of the State Administration of Radio Film and Television Award in 2004, the First Prize of the Ministry of Education Science and Technology Progress Award in 2006, the Second Prize of the National Science and Technology Award in 2007, and the Wang Xuan News Technology Award and the Chia Tai Teaching Award in 2008. He received the Government Allowance granted by the State Council in 2009. He received the Distinguished Doctoral Dissertation Advisor Award from Peking University in 2012 and 2013.